This is an especially important case because the events of the last 100 million years are the most accurately dated and because the several available geologic time scales (*17–19*) are nearly identical for this interval (Table 1). The goodness of fit at the 0.038 per million years frequency is a striking 0.46 million years, which is stronger than all but one of 5000 random simulations run for the four-event case ($P < 0.0002$).

We conclude that the claim for a stationary periodicity with a spacing of approximately 26 million years is strong enough to merit further search for confirming evidence. Because we are dealing with statistical inference in a complex situation, completely satisfactory conclusions will be reached only with higher resolution data on extinction and on other relevant aspects of biological and geological history.

REFERENCES AND NOTES

1. A. G. Fischer and M. A. Arthur, *Soc. Econ. Paleontol. Mineral. Spec. Publ.* 25 (1977), p. 19.
2. D. M. Raup and J. J. Sepkoski, Jr., *Proc. Natl. Acad. Sci. U.S.A.* **81**, 801 (1984).
3. M. R. Rampino and R. B. Stothers, *Nature (London)* **308**, 709 (1984); *Science* **226**, 1427 (1984).
4. See A. Hallam, *Nature (London)* **308**, 686 (1984); R. A. Kerr, *Science* **227**, 1451 (1985); J. Maddox, *Nature (London)* **315**, 627 (1985).
5. A. Hoffman and J. Ghiold, *Geol. Mag.* **122**, 1 (1984); A. Hoffman, *Nature (London)* **315**, 659 (1985).
6. G. B. Wilson, *Nature (London)* **315**, 272 (1985).
7. For percent of familial extinction, 1 standard error on either side of the observed value can be estimated approximately as $[(E_i/D_i)^{1/2} \pm (1/(4D_i))^{1/2}]^2$, where E_i is the number of extinctions in the ith stage and D_i is the standing diversity (assumed to be without error). See Sepkoski and Raup (*8*) for details.
8. J. J. Sepkoski, Jr., and D. M. Raup, in *Dynamics of Extinction*, D. Elliott, Ed. (Wiley, Somerset, NJ, 1986), pp. 3–36.
9. We note that these eight maxima are separated by an average of approximately five stages, which may be the source of J. A. Kitchell and D. Pena's [*Science* **226**, 689 (1984)] calculated "pseudoperiodicity" of 31 million years (= 5 stages × 6.2 million year average duration per stage).
10. J. J. Sepkoski, Jr., in *Pattern and Process in the History of Life*, D. Jablonski and D. M. Raup, Eds. (Springer, Berlin, in press).
11. For generic data, error bars are computed as follows: for high-resolution data, standard errors of estimate were computed as in (*7*); for low-resolution data, assumed 99 percent confidence limits were computed as the difference between a given stage containing all distributed data and no distributed data. The error bar on each side of the observed percentage of generic extinction was thus estimated as the value for the high-resolution data plus one-third the value of low-resolution data.
12. S. M. Stanley, *Macroevolution: Pattern and Process* (Freeman, San Francisco, 1979); ——, in *Extinctions*, M. H. Nitecki, Ed. (Univ. of Chicago Press, Chicago, 1984), p. 69; *Geology* **12**, 205 (1984); —— and L. D. Campbell, *Nature (London)* **293**, 457 (1981).
13. Standard methods of time-series analysis that would fit regular functions to the extinction data are of dubious value also because there is no reason to assume any pattern in the magnitudes (as opposed to timing) of the events and because extinction intensities during events may not be continuous with background intensities.
14. R. B. Stothers, *Astron. Astrophys.* 77, 121 (1979). Stothers assumed that, given the event times t_i, for $i = 1, \ldots, n$, they can be modeled by the equation $t_i = t_0 + j_iP + e_i$, where P is the period, t_0 is the phase, and j_i is the integer value that minimizes the square of $e_i = t_i - t_0 - j_iP$, where e_i is the error term. Values of $[\Sigma_{i=1}^{h} e_i^2/(n - 1)]^{1/2}$ are plotted in Fig. 2.
15. We empirically generated the distribution of the error term (*14*) for each frequency ($1/P$) by randomly locating the n events among the geologic stages. However, because the actual data cannot reveal extinction events in contiguous stages, randomizations were constrained so that only one event could fall in any given stage, and adjacent events were separated by at least one stage without an event.
16. P. H. Signor III and J. H. Lipps, in *Geological Implications of Impacts of Large Asteroids and Comets on the Earth*, L. T. Silver and P. H. Silver, Eds. (Geological Society of America, Boulder, CO, 1982), p. 291.
17. W. B. Harland, A. V. Cox, P. G. Llewellyn, C. A. G. Picton, A. G. Smith, R. Walters, *A Geologic Time Scale* (Cambridge Univ. Press, Cambridge, England, 1980).
18. G. S. Odin, Ed. *Numerical Dating in Stratigraphy* (Wiley, Somerset, NJ, 1982).
19. For "DNAG" time scale, see A. R. Palmer, *Geology* 11, 503 (1983).

20. Supported by NASA grants NAG-237 and NAG-282. We thank A. Hallam, D. Jablonski, S. M. Stigler, S. Tremaine, and three anonymous reviewers for helpful discussions and criticism.

5 August 1985; accepted 10 December 1985

Thermal Spectrum of Uranus: Implications for Large Helium Abundance

GLENN S. ORTON

An analysis of the infrared spectrum of Uranus' disk between 7 micrometers and 3 millimeters suggests a volume mixing ratio for helium in the atmosphere of 40 ± 20 percent, more than for the sun, Jupiter, or Saturn. Alternative explanations require even more extreme assumptions regarding gas abundances or aerosol vertical distribution and spectral properties. The most serious difficulty with a model containing large amounts of helium is devising a credible evolutionary or chemical model explaining the absence or segregation of so much hydrogen.

MANY OF THE RECENT EARTH-based observations of the thermal spectrum of Uranus between 7 μm and 3 mm (*1–5*) were inspired by the need to support the upcoming Voyager 2 investigation of the atmosphere by providing observations of the spectrum where the spacecraft infrared experiment (IRIS) is not sensitive. I undertook an examination of these data to derive a provisional model for the disk-averaged temperature and composition and to evaluate the influence of clouds on the outgoing thermal radiance spectrum. The results of the analysis were surprising because they imply a bulk gas composition very unlike those of Jupiter or Saturn.

Data. All the data used in this study are shown in Fig. 1. No data were used with observational uncertainty greater than 3.5 K, and data were generally excluded whose spectral resolution ($\lambda/\Delta\lambda$) was less than 1.7; some nearly coincident observations (*2, 3*) were averaged together. The newest data in the 400- to 1400-cm^{-1} range (*5*) are consistent with earlier filtered radiometry (*6, 7*) in the same spectral region. The outline of H_2 collision-induced absorption is apparent with a broad translational band near 100 cm^{-1} and strong rotational lines, $S(0)$ and $S(1)$, located, respectively, near 365 and 600 cm^{-1}; double transitions are also located near 950 and 1200 cm^{-1}. As appropriate, data were recalibrated in the following ways. A 1-bar equatorial radius of 25,563 km was adopted uniformly (*2–4*). The observations, with Mars used for absolute calibration (*2–4*), were revised through an improved thermophysical model to predict the outgoing thermal radiance of that planet (*8*). The calibration of other observations was modified, consistent with a recent revision of the infrared stellar flux scale (*9*). The effect of the recalibrations is to bring different data sets into closer agreement with each other, although the major conclusions of this research would be unchanged without the recalibration. However, it does decrease the bolometric thermal output to be equivalent to an effective temperature of 57.7 ± 2.0 K as compared to an earlier estimate of 58.3 ± 2.0 K (*3*).

Model procedure. Recovery of the temperature was possible between about 40 mbar and 8 bars total pressure. The opacity of H_2 induced by collisions with H_2, He, and CH_4 was modeled by ab initio calculations that should be accurate in the relevant temperature range (about 50 to 150 K) within 5 percent throughout most of the spectrum and 15 percent at high frequencies, with relative accuracy much better than these values (*10*). The influence of discrete dimer

Earth and Space Sciences Division, Jet Propulsion Laboratory, California Institute of Technology, Pasadena 91109.

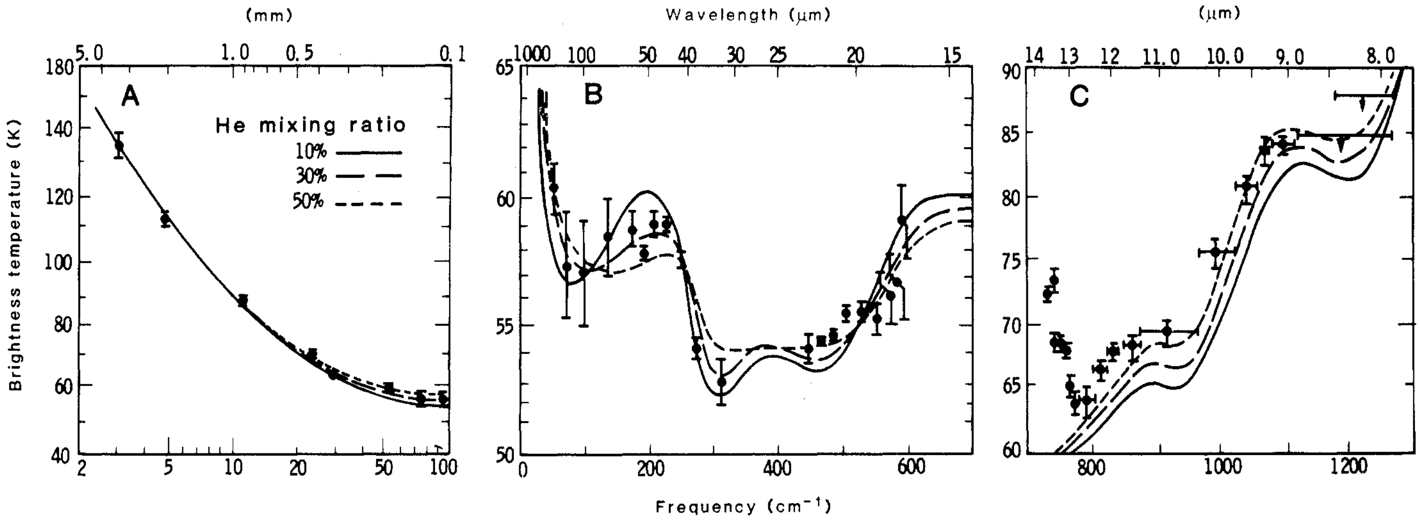

Fig. 1. Brightness temperature data used in this study. Note the different scales of the ordinate in (A), (B), and (C). Upper limits, shown by vertical arrows, correspond to 3-standard-deviation uncertainties. Ostensible features in the 440- to 600-cm^{-1} range are suspect because of imperfect compensation for telluric water vapor absorption, but the general increase of brightness temperatures with frequency is real. Vertical bars represent observational uncertainties only; other systematic uncertainties are estimated as no greater than 15 percent of the observed radiance. Curves represent spectra of models with various mixing ratios of He as indicated, derived without constraint from data in the 860- to 1100-cm^{-1} region. No attempt was made to model emission from C_2H_2 or C_2H_6 in the range of 700 to 860 cm^{-1} nor CH_4 absorption at frequencies greater than 1100 cm^{-1}.

transitions was omitted from the absorption model; they will influence principally the spectral regions near the rotation line centers and the submillimeter through millimeter region. Differences between the shapes of the H_2–H_2 and H_2–He collision-induced absorption spectra have been used to recover the relative abundances of H_2 and He in Jupiter and Saturn from Voyager IRIS observations of Jupiter (*11*) and Saturn (*12*), simultaneous with recovery of the temperature structure. Figure 1 shows the application of this technique to these data for frequencies less than 600 cm^{-1}, with a formal best fit of 35 ± 15 percent for the mixing ratio of He. The uncertainty includes both fitting errors and systematic effects, as detailed below. Substantial excursions from the assumptions of 2 percent CH_4 mixing ratio in the deep atmosphere and equilibrium mixtures of the *para*-H_2 versus *ortho*-H_2 at the ambient temperature do not influence the He abundance determination significantly. Neither do variations in the thermal profile at pressures less than 40 mbar. Note that the spectrum for frequencies greater than 700 cm^{-1} is also sensitive to the relative abundances of H_2 and He. When the data between 860 and 1100 cm^{-1} are also considered (avoiding regions of possible absorption or emission by hydrocarbons), a best fit of 40 ± 20 percent is derived. From these data in Fig. 1C, it is clear that this spectral region considered alone would be matched even better by a He abundance higher than 40 percent.

The temperature structures derived from the models are shown for the 10 percent He and the 40 percent He cases in Fig. 2A. This figure also shows the dependence on the shape of the temperature profile overlying the 40-mbar level, using perturbations of radiative equilibrium profiles (*13, 14*). Figure 2B illustrates the dependence of the disk-averaged brightness temperature spectrum on the shape of the stratospheric temperature structure. Note that the assumption of relatively warm overlying temperatures (solid and long-dashed curves in Fig. 2) are effective in suppressing emission originating from the $S(0)$ line center near 365 cm^{-1}. This is consistent with the absence of an observed feature in preliminary spectral data from this region (*15*).

The high value derived for the helium mixing ratio was unexpected, although the possibility was suggested earlier (*6*). An assessment of the potential systematic uncertainties associated with the data included use of the old calibration, exclusion of portions of the data, imposition of brightness temperature offsets on entire data sets (*2, 4*) near 200 cm^{-1} by as much as 2.0 K, and "conspiratorial" arrangements of data within their uncertainty limits to offset the derived mixing ratio systematically toward higher or lower values. The 20 percent uncertainty for the mixing ratio quoted above was derived from this assessment. The validity of a model with only 10 percent He by volume (more typical of the sun, Jupiter, and Saturn) could be preserved by relying on one of the following systematic problems with the data. (i) The calibration of Mars must be low by 35 percent near 200 cm^{-1} in a manner that mimics the shape of the 10 percent He spectrum as shown. The redundancy of information is such that by excluding data below 200 cm^{-1} and relying instead on data in the range 860 to 1100 cm^{-1}, radiances are derived that are 35 percent higher than observed (near 65 K in brightness temperature around 100 to 200 cm^{-1}). (ii) The calibration of the data in the range 860 to 1100 cm^{-1} is high by a factor of 5. (iii) The collision-induced absorption of H_2–He must be low by 50 percent near 200 cm^{-1} in a manner that distorts the spectrum, the 1000-cm^{-1} region of the absorption spectrum is too high by about a factor of 3, or the entire absorption spectrum is a factor of 4 too low. None of these is reasonable.

Since its presence is only inferential, another species could be substituted for He if the absorption spectrum it induces by colliding with H_2 is stronger near 200 cm^{-1} and weaker near 800 to 1200 cm^{-1} compared with H_2 itself. Even better, if its spectrum were intrinsically stronger than H_2–He, there would not need to be as much of it mixed in the atmosphere. Any substance heavier than H_2 tends to have narrower rotational line widths; thus the 1000-cm^{-1} opacity on the high-frequency wing of the $S(1)$ line should be smaller. The (H_2)–H_2 (dimer-monomer) spectrum should be similar to that of H_2–He, but, at most, only about 1 to 2 percent of molecular hydrogen should be in the dimer state for the gas densities in question (*10*). Individual dimer transitions not included in the model do not exert much influence over the spectral regions in question. Stevensen (*16*) expects a molar fraction of about 1 percent N_2 if all the nitrogen in the outermost atmosphere is quenched in the diatomic molecular state.

The rotational lines of H_2–N_2 are factors of tens stronger than H_2–He, but the absorption near 200 and 1000 cm^{-1} is only about three times as strong. Thus, one could substitute for only about 3 percent of the inferred helium this way, even ignoring the different shape of the spectrum near 200 to 360 cm^{-1}. Methane would also do well, but H_2–CH_4 absorption is already included in the model explicitly. To be more effective, it would need to be distributed several scale heights above its nominal condensation level. Other candidate species such as Ar, HD, or even CO might do well spectrally, but are either observed or expected to be many orders of magnitude less abundant than required to produce the needed opacity. Therefore, I conclude that there is no simple gaseous substitute for helium.

Effects of clouds and aerosols. Use of this type of spectral shape analysis by the Voyager IRIS investigation at Jupiter and Saturn (*11, 12*) precluded the use of locations where cloud particles might influence the outgoing thermal radiance significantly. Figure 3 shows the influence on the spectrum of a cloud of 10-μm CH_4 particles which produces the same spectral shape as the addition of He. It is much more difficult to get sufficient quantities of 1-μm particles to do as well, and at least some particles must be distributed above the 800-mbar level to be effective. However, the optical thickness of this cloud is very much larger than allowed by analysis of the reflection properties of the atmosphere at wavelengths less than 1 μm (*17*). Furthermore, the cloud does not help the model at higher frequencies, as shown in Fig. 3B. The thermal spectrum is suppressed even further, and the reflected solar spectrum, previously invoked to match the filtered radiometric observations (*6*), is far too bright for frequencies greater than 1000 cm^{-1}. Invoking atmospheric absorption by CH_4 near 1300 cm^{-1} is ineffective because the reflecting particles are distributed above the level where CH_4 is rapidly depleted by condensation. Even if the particles are made arbitrarily unable to reflect sunlight, they will suppress the spectrum, as shown in Fig. 3C (solid curve).

If the particles effective at 200 cm^{-1} do not somehow exert any influence on the spectrum near 800 to 1200 cm^{-1}, a source of spectrally continuous emission can reconcile the radiances of the 10 percent He model with the higher radiance values observed. Figure 3C shows that an emitting layer near 150 K in the stratosphere will fit the observed spectrum, particularly if the optical thickness of the layer depends on the fourth power of the frequency. The shape is not matched as well with a linear dependence, nor with temperatures as low as 100 K, nor in the presence of tropospheric absorption given by the solid curve in Fig. 3C.

Thus, appealing to atmospheric cloud and aerosol properties to provide a better match to the spectrum with a 10 percent He mixing ratio model results in two arbitrary fixes for the two spectral regions in question. Tropospheric cloud particles near 800 mbar must be optically thick near 200 cm^{-1}, almost invisible near 800 to 1200 cm^{-1}, and optically thin (0.4 to 1.0) near 0.7 μm (*17*). In addition, there must be a layer of stratospheric aerosols that are efficient radiators at levels corresponding to temperatures of 150 K or more in the stratosphere. As a whole, the clouds are needlessly complicated inventions, providing arbitrary fixes to specific problems with only marginal relevance to constraints imposed by other spectral regions.

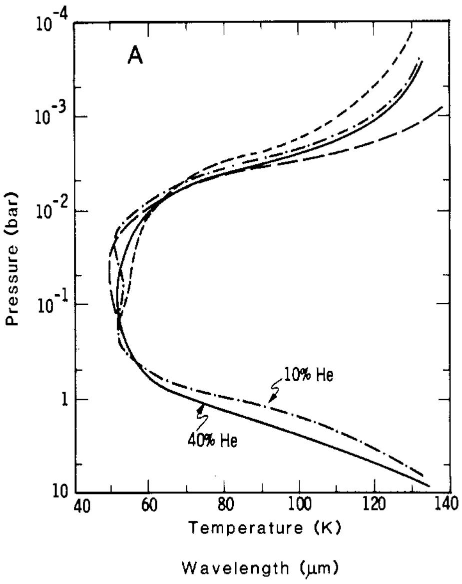

Fig. 2. (A) Temperature structure derived from inversion of the spectral data shown in Fig. 1. Different assumptions about the shape of the overlying stratospheric temperature profile are illustrated for the 40 percent He case by the solid, long-dashed and short-dashed curves. The alternating dot-dashed curve corresponds to the solid curve, except for the assumption of 10 percent He. Its spectrum is shown by the short-dashed curve in Fig. 1. (B) Spectra for the 40 percent He temperature structures shown in (A). Each is keyed to the identical symbol for its corresponding temperature structure.

The case against helium. Few, if any, observable constraints discriminate against a model with 40 percent helium. Interior models (*18, 19*) could possess an outer envelope even more than twice the density of hydrogen. The mixture of 40 percent He would change the mean molecular weight of this envelope from 2.2, a value consistent with solar abundances above the CH_4 condensation level, to values closer to 2.6 to 2.85. These, in turn, would raise an atmospheric temperature of 150 K inferred from analysis of stellar occultation data (*14*, figure 19) to values in the range 177 to 194 K. Nevertheless, the presence of even very small amounts of insolation-absorbing aerosols in this part of the atmosphere should be sufficient to raise the temperature of an atmosphere in radiative equilibrium to these temperatures without violating constraints imposed by the solar reflectivity spectrum (*13*).

The shape and depth of near-infrared H_2 quadrupole lines are sensitive to conditions of pressure and temperature of line formation as well as to the optical path of H_2 transversed (*17*). Analysis of high-resolution observations of these lines for the conditions given in the He-rich models reported here shows that they can be matched provisionally as well as models with only 10 percent He. This is partly a result of the fact that the temperature structure given by this work is warmer than the one assumed originally (*13*). The conditions required for the best model fit include the assumption that all H_2 *para* and *ortho* states are in equilibrium with the ambient temperature and that an optically thick cloud top is located at pressures exceeding about 5 bars, rather than 2.4 to 3.2 bars derived from the 10 percent He model (*17*).

The greatest difficulty with large amounts of helium in the present atmosphere of Uranus lies in understanding how it could separate from hydrogen. If H or H_2 is lost hydrodynamically or by diffusive escape early in Uranus' history, the process would need to be so efficient that He would easily be transported along with it, unless Uranus' gaseous atmosphere (H_2 and He) is actually quite thin (*20, 21*). Helium could be redistributed preferentially in the outer envelope of the atmosphere if a large ionic ocean of water existed in the interior in which H_2 were far more soluble than He. While there are few data or theories relevant to this speculation, initial indications of the differential solubility of H_2 and He would not alone justify the He abundance inferred from the infrared spectrum (*19*). Hydrogen could, alternatively, escape detection by be-

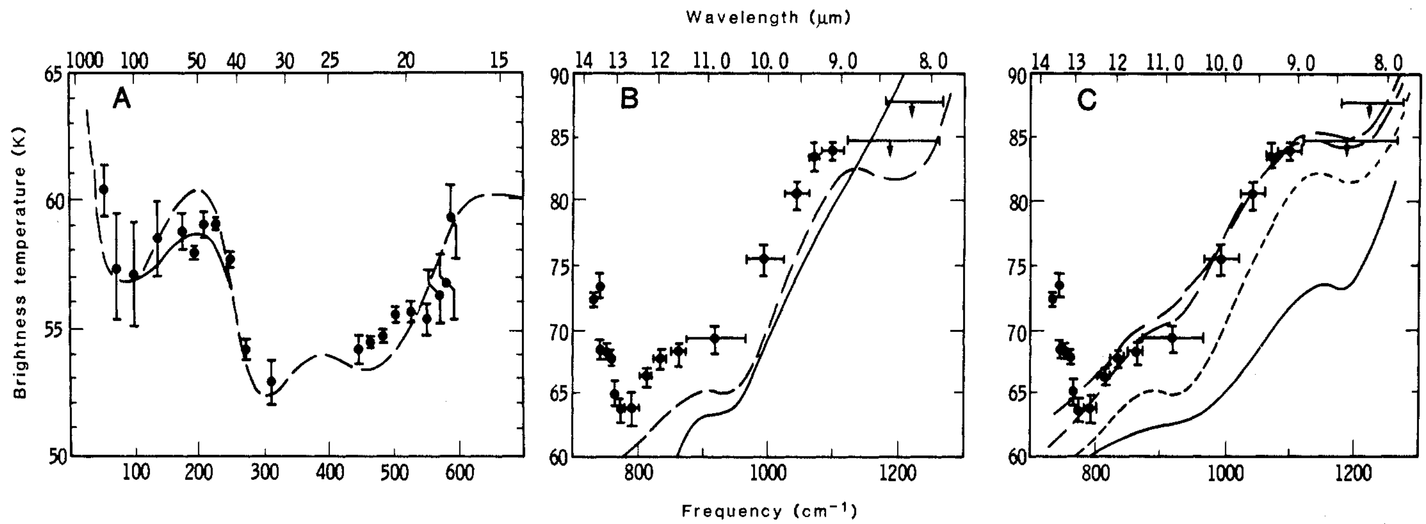

Fig. 3. Spectra of atmospheric models with various clouds. The long-dashed curves in (A) and (B) correspond to the 10 percent He model spectrum of Fig. 1 for clear atmospheric conditions. (A) The spectrum under the influence of a cloud of 10-μm CH_4 particles, distributed from 1 bar (close to the condensation level for mixing ratios between 0.2 and 4 percent in the deep atmosphere) to 400 mbar (a probable boundary for upwelling convective activity) with scale height 0.15 times the gas scale height (similar to an adiabatic cloud). The quantity of CH_4 required to match the observed spectrum is well below the limits imposed by mass balance constraints. (B) The spectrum of such a cloud at higher frequencies including the effects of reflected sunlight. The spectrum is too dim at frequencies less than 1000 cm^{-1} and too bright at higher frequencies. (C) (Solid curve) Spectrum of such a cloud if particles reflected no sunlight and (long-dashed curves) spectrum if this cloud exerted no influence in this spectral region and an emitting layer existed at the 150 K region of the stratosphere. The optical thickness of the layer is 6×10^{-5} at 1000 cm^{-1}, and curves are shown for linear and fourth-power dependence on frequency. Such a layer provides a satisfactory fit to the data, but would not work for lower temperatures or in the presence of a dark tropospheric cloud.

ing chemically bound in the interior to heavier atoms (*19, 22*). For example, if all the carbon and all the oxygen presently in Uranus arrived without being attached to H atoms and is now chemically saturated as CH_4 and H_2O, then the final He mixing ratio could be enhanced by 1.1 to 3.5 (*22*) over a value corresponding to solar abundance (roughly 15 percent). Although this prediction significantly overlaps the range of uncertainty implied by this investigation, matching the nominal value of 40 percent would require the dissolution of a very large fraction of the solid material that helped to form Uranus in its gaseous envelope. Stevenson (*19*) believes that 2.4, again within the range of uncertainty, should be regarded as an upper limit, as it is predicated on the assumptions that 50 to 60 percent of Uranus' mass is in the nongaseous form and only 7 to 10 percent is in gaseous form (that is, H_2 and He).

Conclusions. The infrared spectrum of Uranus, notwithstanding unforeseen systematic errors, implies a helium mixing ratio in the range of 20 to 60 percent. Other gaseous candidates that could mimic the influence of He on the spectrum are unlikely to be found in sufficient abundance. The next most likely explanation involves particle layers requiring rather special properties that are generally inconsistent with constraints imposed by the observed spectral reflectivity of the atmosphere. On the other hand, the presence of so much helium, although not contradicted by observable evidence, is extremely difficult to explain with our current understanding of physical and chemical processes acting during formation and operating in the present interior of the planet.

Further constraints can be found for the atmospheric model. The influence of bound-bound and bound-free dimer opacities omitted from the current absorption model must be included. Quantitative estimates should be given for the influence of He on the H_2 quadrupole line shape and comparisons made with the observations. The comparison between Voyager 2 radio occultation and infrared probing of the atmosphere will be used to determine a mean molecular weight (*11, 12*), although some ambiguity will remain between the molar fractions of helium and molecular nitrogen. The IRIS measurements will refine the shape of the spectrum near 200 to 300 cm^{-1}. Finally, the general appearance of the temperature structure determined by the radio subsystem occultation experiment may be used to make first-order distinctions between models, such as those shown in Fig. 2A where the lapse rate is positive and substantial.

A relatively large helium abundance represents the most straightforward means for understanding the available data. However, should the relative abundances of H_2 and He be solar-like, then I maintain that the infrared spectrum of Uranus is implying something unusual about the composition or cloud properties.

Note added in proof: Preliminary Voyager 2 results show that IRIS spectra alone and a comparison of IRIS and radio occultation results indicate a He mixing ratio of 12 ± 4 percent. In addition, IRIS results in the spectral range of about 200 to 300 cm^{-1} appear consistent with the data shown above. These results argue for the following conclusions. (i) The model of a warm stratospheric haze raising the 7- to 14-μm spectral continuum should be considered likely. (ii) Radiances between about 20 and 60 cm^{-1} are higher than the model by some 5 to 10 percent. Presuming that a CH_4 cloud is unlikely to be suppressing 200-cm^{-1} radiances, as I suggested, the opacity model or the calibration is incorrect at 20 to 60 cm^{-1}. The relative spectral errors for both H_2–H_2 and H_2–He opacity models should be examined more carefully in this region, although they appear to represent laboratory data at 77.4 K rather well. Similarly, the thermophysical model of Mars used as a calibration standard in this spectral region should be examined for potential systematic errors, although significant changes in the model would be needed to accumulate systematic errors of the size required going from 200 cm^{-1} to shorter frequencies. Finally, the possibility of other opacity sources in this spectral region must also be explored more thoroughly.

REFERENCES AND NOTES

1. B. L. Ulich, J. H. Davis, J. M. Hollis. *IEEE Trans. Antennas Propag.* **AP28**, 367 (1980).
2. R. H. Hildebrand *et al.*, *Icarus* **64**, 64 (1985).

3. G. S. Orton, *et al.*, *ibid.*, in press.
4. S. H. Moseley, B. J. Conrath, R. F. Silverberg, *Astrophys. J.* **292**, L43 (1985).
5. D. Aitken *et al.*, in preparation.
6. A. T. Tokunaga, G. S. Orton, J. Caldwell, *Icarus* **53**, 141 (1983).
7. G. S. Orton, A. T. Tokunaga, J. Caldwell, *ibid.* **56**, 147 (1983).
8. P. Christensen and B. Jakosky, in preparation. Christensen provided predicted model radiances for the dates, times, and spectral ranges corresponding to the observations cited in (*2–4*). Their model is based on physical properties of Mars derived from Viking infrared maps and on Earth-based microwave data, and it accounts explicitly for rotational variability.
9. G. H. Rieke, M. J. Lebovsky, F. J. Low, *Astron. J.* **90**, 900 (1985).
10. J. Borysow, L. Trafton, L. Frommhold, G. Birnbaum, in preparation; W. Meyer, L. Frommhold, G. Birnbaum, in preparation; A. Borysow and L. Frommhold, *Astrophys. J.*, in press; A. Borysow and L. Frommhold, *ibid.*, in press. Frommhold and A. Borysow provided appropriate models replicating the ab initio results for H_2 absorption induced by collisions with the various gases cited here.
11. D. Gautier *et al.*, *J. Geophys. Res.* **86**, 8713 (1981).
12. B. J. Conrath, D. Gautier, R. A. Hanel, J. Hornstein, *Astrophys. J.* **202**, 807 (1984).
13. J. Appleby, *Icarus*, in press; personal communication.
14. G. S. Orton and J. F. Appleby, *NASA Conf. Publ.* **2330** (1984), pp. 89–156.
15. S. H. Moseley, W. Glaccum, R. Silverberg, B. Conrath, R. Loewenstein, in preparation; S. H. Moseley, W. Glaccum, B. Conrath, R. Loewenstein, G. Orton, in preparation. These airborne and ground-based spectrometric data cover the range 18 to 38 μm.
16. D. J. Stevensen, *Bull. Am. Astron. Soc.* **16**, 658 (1984).
17. K. H. Baines and J. T. Bergstralh, *Icarus*, in press; K. Baines (personal communication) calculated conditions matching the observed H_2 quadrupole for the composition and temperature environment described here.
18. W. B. Hubbard, *NASA Conf. Publ. 2330* (1984), pp. 291–326; personal communication.
19. D. J. Stevensen (personal communication) surveyed alternative physical and chemical models for the evolution and interior of Uranus.
20. D. M. Hunten. *J. Atmos. Sci.* **30**, 1481 (1973).
21. D. M. Hunten. *Bull. Am. Astron. Soc.* **17**, 702 (1985).
22. J. B. Pollack, M. Podolak, P. Bodenheimer, *Bull. Am. Astron. Soc.* **17**, 702 (1985); J. Pollack, personal communication.
23. I thank everyone whose conversations have helped shape the direction of this work. I especially thank D. Aitken and my collaborators for allowing me to use our observations here before our own report. I ask the forebearance of the reader with respect to the number of citations of personal communications and publications "in preparation" or "in press." This was predicated by use of very recent data and the dearth of published discussion on enhanced He abundances in the outer solar system. I thank J. Appleby and J. Bergstralh for editorial suggestions. Supported by the Planetary Atmospheres Program of the NASA Office of Space Sciences and Applications under NASA contract NAS 7-100.

29 November 1985; accepted 23 January 1986

Maturational Changes in Cerebral Function in Infants Determined by ^{18}FDG Positron Emission Tomography

HARRY T. CHUGANI* AND MICHAEL E. PHELPS

2-Deoxy-2[^{18}F]fluoro-D-glucose positron emission tomography performed in human infants during development revealed progressive changes in local cerebral glucose utilization. In infants 5 weeks of age and younger, glucose utilization was highest in the sensorimotor cortex, thalamus, midbrain-brainstem, and cerebellar vermis. By 3 months, glucose metabolic activity had increased in the parietal, temporal, and occipital cortices and the basal ganglia, with subsequent increases in frontal and various association regions occurring by 8 months. These functional changes measured with positron emission tomography are in agreement with behavioral, neurophysiological, and anatomical alterations known to occur during infant development.

SINCE GLUCOSE AND OXYGEN ARE the principal substrates for meeting the energy demands of the brain, measurements of the rates at which these substrates are utilized provide an assessment of the level of neuronal function in the brain. Measurement of the rates of regional substrate utilization in the brain during maturation provide a means whereby local functional activity can be related to various stages of behavioral development. Previous investigations of changing metabolic patterns in the maturing brain of animals (*1*) and humans (*2–4*) have involved the Kety-Schmidt method (*5*), which estimates average rates of blood flow and substrate utilization for the brain as a whole. Subsequently, measurements of local cerebral blood flow (LCBF) by quantitative autoradiography (*6*) permitted indirect assessment of local cerebral metabolic activity during development (*7*) because of the close relation between LCBF and local cerebral metabolic activity (*8*). With the introduction of the 2-deoxyglucose method for determining the local cerebral metabolic rate for glucose (LCMRglc) in animals (*9*), a number of investigators directly measured local changes in glucose utilization in the developing brain of the dog (*10*), monkey (*11, 12*), and sheep (*13*). However, the lack of a suitable noninvasive method precluded the measurement of LCBF and LCMRglc in the developing human brain.

Positron emission tomography (PET) (*14*), which involves tracer kinetic measurements of compounds labeled with positron-emitting isotopes, provides a noninvasive approach with which the principles of the 2-deoxyglucose method can be directly applied in humans to visualize and quantify LCMRglc (*15*) during postnatal development. In using PET with 2-deoxy-2[^{18}F]-fluoro-D-glucose (FDG) to measure LCMRglc in infants with certain neurological disorders, we obtained valuable data on LCMRglc during development. Although our studies were conducted in infants who were not completely normal, we believe that the data are reasonably representative of the normal state because all these infants had episodic neurological events but remained neurodevelopmentally normal (follow-up period, 8 to 14 months).

All studies were performed in accordance with the policies of the UCLA Human Subject Protection Committee. From over 60 infants and children who had been measured for LCMRglc, we selected nine infants whose status at the time of the procedure was judged to be nearly normal (Table 1).

In infants 5 weeks of age and younger ($n = 4$), LCMRglc was highest in the sensorimotor cortex, thalamus, midbrain-brainstem (*16*), and cerebellum (particularly the vermis, the centrally located, phylogenetically older portion of the cerebellum) (Fig. 1). The rate of glucose utilization was very low in the basal ganglia and the remaining cortex. By about 3 months of age ($n = 2$), a relative increase in LCMRglc was noted in much of the cerebral cortex, and LCMRglc in the striatum approached that of the thalamus. Glucose utilization in the cerebellum, previously highest in the vermis, now also extended laterally into the hemispheres. The frontal cortex and several association cortical regions, however, remained less metabolically active than the rest of the brain. A pattern of glucose utilization resembling that seen in adults (*17*), with prominent activity in frontal and association cortices, was established in infants 7.5 months, 1 year, and 1.5 years old.

In Fig. 2 the ratios of local cerebral to thalamic glucose utilization for several selected regions are plotted as a function of age, revealing the marked heterogeneity in the rates of functional maturation for different brain regions. Compared to the thalamus, the caudate and lenticular nuclei were relatively hypometabolic at birth, but LCMRglc rapidly approached that of the thalamus by the third month. The sensori-

H. T. Chugani, Departments of Neurology and Pediatrics, MDCC 22-464, UCLA School of Medicine, Los Angeles 90024.
M. E. Phelps, Division of Nuclear Medicine and Biophysics, UCLA School of Medicine, Los Angeles 90024.

*To whom correspondence should be addressed.